Chemical Engineering Journal 406 (2021) 126856

Contents lists available at ScienceDirect

Chemical Engineering Journal

journal homepage: www.elsevier.com/locate/cej

Nickel-catalyzed formation of mesoporous carbon structure promoted capacitive performance of exhausted biochar

Deping Li[a], Ling Zhao[a,b,*], Xinde Cao[a,b], Ziyue Xiao[c], Hongyan Nan[b], Hao Qiu[b]

[a] China-UK Low Carbon College, Shanghai Jiao Tong University, Shanghai 201306, China
[b] School of Environmental Science and Engineering, Shanghai Jiao Tong University, Shanghai 200240, China
[c] School of Civil and Environmental Engineering, Stanford University, Stanford CA 94305, USA

HIGHLIGHTS

- Waste nickel-laden biochar was reclaimed to produce capacitor material.
- Good capacitance (~190 F g^{-1}) and excellent stability of EDLC material was achieved.
- Ni intensified carbonate decomposition promoting formation of mesoporous structure.
- Ni enhanced carbon layer erosion in KOH activation facilitating mesopores-formation.
- Ni catalyzed sp^3 to sp^2 hybridization benefiting conductivity and stability of EDLC.

GRAPHICAL ABSTRACT

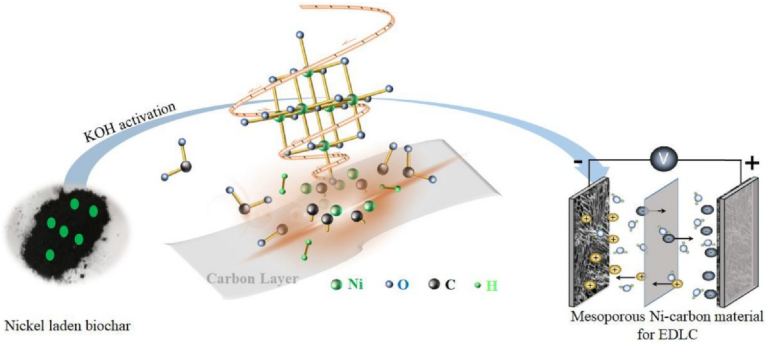

ARTICLE INFO

Keywords:
Exhausted biochar
Heavy metal
Electrical double layer capacitor
Mesoporous structure
Energy intensive material

ABSTRACT

Biochar is widely studied to adsorb heavy metals in wastewater, while the reclamation of exhausted biochar becomes a challenge. In this study, biochar adsorbing Ni^{2+} with two concentration levels were used as precursors to prepare electrical double layer capacitor (EDLC) materials. A good performance of capacitance (188.9 F g^{-1} at 0.5 A g^{-1}) and stability (capacitance retention maintained 95.9% after 1000 cycles) were achieved with the precursor of nickel-laden biochar of 100 mg g^{-1} and activation temperature of 600 °C, while the capacitance of control without nickel was only 98.4 F g^{-1}. Power X-ray diffraction (XRD), Fourier Transform Infrared Spectroscopy (FTIR), Brunauer-Emmete-Teller (BET) and the Raman Imaging combined with Emission Scanning Electron Microscope (RISE) identified that metallic nickel promoted carbonate decomposition and invaded into carbon layer, which assisted mesopores (551.8 m^2 g^{-1}) formation and contributed to a high capacitance. Moreover, nickel catalyzed the transfer of sp^3 carbon to sp^2 hybridization, which enhanced the conductivity and stability of EDLC. This study provides a feasible and simple strategy of reclaiming waste biochar after adsorbing nickel to prepare energy intensive material and implies the possibility and necessity of cascading applications of biowastes from environmental remediation to energy storage.

* Corresponding author at: China-UK Low Carbon College & School of Environmental Science and Engineering, Shanghai Jiao Tong University, Shanghai 201306, China.
E-mail address: wszhaoling@sjtu.edu.cn (L. Zhao).

https://doi.org/10.1016/j.cej.2020.126856
Received 21 July 2020; Received in revised form 26 August 2020; Accepted 27 August 2020
Available online 02 September 2020

1. Introduction

Biochar is a type of carbon-rich material produced from the pyrolytic conversion of organic biowastes in O_2-starved atmosphere at temperature of 300–700 °C, and it finds its position in heavy metals adsorption, soil amelioration and carbon sequestration [1]. It is widely proved that biochar could remove heavy metals (Pb, Cu, Cd, Cr, Ni, etc.) from contaminated water due to its heterogeneous pore structure, abundant surface functional groups and various inherent minerals [2,3]. However, after adsorption, the metals-laden biochar has exerted another threat on the environment because there has not sufficient attention been paid to it until now. If this exhausted biochar was carelessly disposed, it would cause secondary pollution in the environment, especially under acidic conditions [4]. Some researchers tried to reuse biochar multiple times by eluting it with acid or alkali [5–8], but it left the final disposal problem of waste biochar behind. Therefore, how to reutilize the biochar after absorbing heavy metals has become a challenge.

Previous studies have shown that biochar adsorbed with heavy metal Ni^{2+} [9], Cu^{2+} [10] can be used to create pseudo-capacitors, and the heavy metals were oxidized to their oxides by microwave, thermal annealing, etc. Hao et al used carbon nanotube to absorbing Cr^{6+} or Cu^{2+} from contaminated water and transfer the residues to pseudo-capacitors materials by pyrolysis at 800 °C [11]. However, their capacitance and energy density were generally limited, and their methods were only focus on heavy metals. In those studies, as most of the heavy metals have enough electron for electricity storage, capacitive performances of the recovered materials mainly depended on the pseudo-capacitance of metal oxide while the porous structure of the carbon materials was ignored. Since the level of graphitization and pore structure of carbon material have a great influence on the conductivity and mass transfer resistance of the material when it is used as a capacitor [12–14], the structural change of carbon material should also be fully considered in the research. Therefore, only in the cases that both the heavy metals and the carbon matrix play important roles in the capacitive performances, could the multiple applications of biochar as adsorbent, carbon sequestration materials and energy storage materials be realized.

Porous carbon materials are often used for preparation of EDLC. The main functional unit is the mesoporous carbon structure which leads to a low ion diffusion resistance [15,16], and can be prepared by activating biomass or biochar with KOH under thermal treatment [17,18]. The porous carbon with a huge mesoporous volume or large specific surface area provides more adsorption sites for the anion and cations, thus forming a stable layer capacitance [19]. For example, Mijailović et al prepared activated carbon from hemp fiber at 900 °C, it showed a capacitive performance of 122 F g^{-1} at 5 mV s^{-1} and the specific surface area of mesoporous was 40 m^2 g^{-1} [20], while activated carbon prepared by Saha et al with lignin at 1000 °C had a capacitive performance of 102 F g^{-1} at 1 mV s^{-1} and the mesoporous volume was 0.66 cm^3 g^{-1} [21]. Even when the few layer graphene was prepared by cumbersome processing with the precursor of peanut shell, its capacitance was still low (186 F g^{-1}) and furthermore the capacitance for active carbon derived from peanut shell was less than 50 F g^{-1} [22]. In most of these studies, the mesopores of the materials were limited, indicating that a trade-off between micropores and mesopores was difficult to be achieved via traditional activation of biomass or biochar with typical chemicals or gases.

Presence of inorganic elements such as minerals (alkali, alkaline earth metals and transition metals) in the biomass precursors have remarkable influences on pyrolysis process since they are closely related to carbon decomposition, molecules breaking and carbon polymerization [23]. Alkali and alkaline earth metals including K, Na, Ca and Mg have been widely investigated in biomass pyrolyzation. It is found that the presence of those metals lowered the temperature of initializing carbon decomposition, promoted the release of small organic molecules and augmented the turbostratic carbon structure [24–26]. Cobalt, as a transition metal, has similar properties and chemical behaviors with nickel and iron. It has been proven that a small amount of Co^{2+} could promote the KOH activation process, facilitating the formation of mesopores and graphite structure [27,28]. It was assumed that Co^{2+} might catalyze carbon erosion and lead to more mesoporous structure [14]. Therefore, taking full advantage of both inorganic minerals (alkaline earth metals, transition metal) and carbon matrix from heavy metal-laden biochar in producing metal–carbon material is sensible and worth exploring. In addition, the composite metal–carbon materials have great potential to act as precursors for producing gas storage materials, separation medium, sensors and supercapacitors [29–31].

Nickel is an industrial heavy metal, which is often found in wastewater such as electroplating water existing as a wide concentration range. Biochar could be used as a low-cost and high-efficiency adsorbent to remove Ni^{2+} from the wastewater. This study chose biochar coated with Ni to conduct the reutilization process and test the feasibility of preparing EDLC material. Firstly, influences of process parameters on capacitive performance of the EDLC materials were identified, which took into account the Ni^{2+} loading concentrations and activated temperatures; Secondly, further exploration of capacitive performances under different electricity-voltage conditions was performed; Thirdly, and the most important, mechanisms were revealed regarding to formation of porous structure, the hybridization of carbon atoms around nickel particles, and interaction of nickel and carbon with assistance of instruments such as scanning electron microscope (SEM), energy-dispersive spectroscope (EDS), and in situ Raman.

2. Experimental section

2.1. Preparation of nickel-laden biochar

A typical crop biowaste, peanut shell, was chosen to produce biochar, which was collected from Shanghai, China. After being washed, air-dried and crushed, the biowaste was fed into a pyrolysis system with a heating rate of 10 °C min^{-1} under N_2 atmosphere with a flow rate of 200 mL min^{-1}. Temperature was increased to 600 °C and held for 2 h, which was a moderate treatment for biochar production. The biochar product was designated as 'BC6' and its properties were presented (Table S1 and S2, Supporting Information). Then the biochar was used to treat the Ni^{2+} contaminated water ($NiCl_2$ solution), i.e., it was added into the contaminated water with 500 mg L^{-1} and 100 mg L^{-1} Ni^{2+} at a ratio of 1.0 g BC6 to 1000 mL water (Fig. 1). After adjusting pH to 9.0 with 1 M KOH (Yonghua Chemical Technology Co., Ltd), stirring vigorously and holding for 30 min, the solid phases were separated from aqueous solution by centrifugation and dried for 12 h at 60 °C. Here adjusting the pH of the wastewater to 9.0 was to guarantee that all the Ni^{2+} in the wastewater could deposit on the biochar as $Ni(OH)_2$. In the real industrial wastewater treatment, adjusting the pH to a high value as about 9.0 is an effective and commonly used strategy to decrease the metals concentration below a value that is safe for discharging.

2.2. Preparation of EDLC materials from nickel-laden biochar

The recovered Ni-laden biochar was utilized to produce EDLC materials using typical KOH activation method, and three activation temperatures (600 °C, 700 °C and 800 °C) were chosen for the thermal chemical treatment to reconstruct the pore structure of carbon matrix. The detailed process parameters could be seen in Fig. 1. In detail, the recovered biochar was dispersed into deionized water, and the solid KOH was added at 1:3 ($w_{biochar}/w_{KOH}$) into the water with stirring vigorously to dissolve uniformly. Then the mixture was dried for 12 h at 60 °C. The feedstock was placed in a tubular furnace, heated at the speed of 5 °C min^{-1}, and activated for 4 h at 600 °C, 700 °C and 800 °C respectively under N_2 atmosphere [17]. After activation, the materials were rinsed with deionized water and dried at 60 °C. The products were

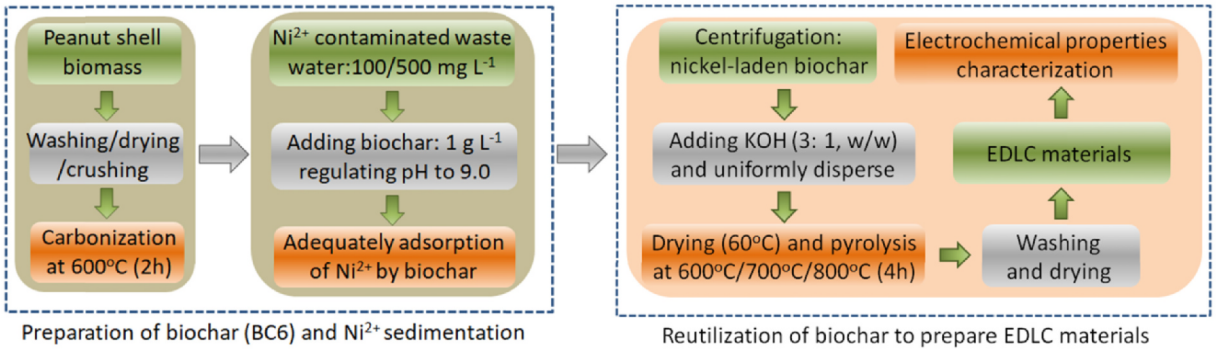

Fig. 1. The preparation process of electrochemical double layer capacitor (EDLC) materials from nickel-laden biochar.

referred to as BC6-Nim-Kn, where the m and n represent the concentration of Ni^{2+} and activation temperature respectively, i.e., for BC6-Ni5-K8, 5 represent the Ni^{2+} concentration of 500 mg L^{-1} and 8 represent activation temperature of 800 °C.

2.3. Electrochemical measurements

The electrochemical properties were tested by a three-electrode system on the electrochemical workstation (Vertex.One, IVIUM, Netherlands). A platinum plate was used as the counter electrode, Hg/HgO as the reference electrode, and the electrolyte was 1 M KOH. The working electrode material was configured by EDLC materials, polytetrafluoroethylene and acetylene black with a ratio of 8:1:1, which was mixed homogeneously to forming a thick paste with the assistance of ethanol. Then the paste was dried and coated on the surface of nickel foam (1 cm × 1 cm), and pressed at 20 Mpa for 2 min [32].

Cyclic voltammetry (CV) curves were obtained with the potential window between −1 V to 0 V, and it reflected the reversibility in charge–discharge process. The galvanostatic charge–discharge (GCD) curve directly reflected the potential platform, the capacitive performance and the current density that a material can withstand [10,11]. The charge–discharge performances of the materials were tested under different current densities, and the capacitance was calculated in three-electrode system by the equation:

$$Cp = \frac{I\Delta t}{m\Delta V} \quad (1)$$

where I is the constant current (A), m is the mass loading (g), Δt refers to the discharge time (s) and ΔV represents the potential window (V) [33].

The electrochemical impedance spectroscopy (EIS) can reflect the conductivity of the material, the electron transfer resistance of the electrode–electrolyte interface and the mass transfer resistance of the liquid phase [34], it was obtained at the frequency range of 0.01 Hz ~ 100 kHz with the voltage of 5 mV.

2.4. Structure characterizations

Power X-ray diffraction (XRD D/max-2200/PC, Rigaku, Japan) with Cu Kα (λ = 1.540598 Å) was conducted to investigate the crystalline structure of nickel-carbon materials from 10° to 80° with the scanning rate of 2° min^{-1}. The surface functional groups were measured by Fourier Transform Infrared Spectroscopy (FTIR, Prestige 21 FTIR, Shimadzu, Japan). Brunauer-Emmete-Teller (BET, JW-BK222, JWGB, China) was used to analyze the porous structure including specific surface area, pore size distribution, and pore volume, etc. The Raman Imaging combined with Emission Scanning Electron Microscope (RISE, TESCAN-MAIA 3 GMU model 2016/WITec apyron, Czech) which is the combination of SEM, EDS and in situ Raman spectroscope, was used to investigate the surface morphologies structure, element distribution and the main hybridization of carbon around the nickel particles.

3. Results and discussion

3.1. Electrochemical properties of EDLC materials

The electrochemical performances of the produced EDLC materials were presented in Fig. 2. The results showed that the EDLC materials with the precursor of biochar absorbed with 100 mgNi^{2+} g^{-1}char obtained higher capacitance than those with the biochar absorbed high Ni^{2+} concentration (500 mgNi^{2+} g^{-1}char) after KOH activation at 600 °C, 700 °C and 800 °C (Fig. 2a, b). The best capacitance of 188.9 F g^{-1} for BC6-Ni1-K6 was achieved based on the GCD curves (Fig. 2c) at the current density of 0.5 A g^{-1}, while the capacitance for BC6-Ni1-K7, BC6-Ni1-K8, BC6-Ni5-K6, BC6-Ni5-K7 and BC6-Ni5-K8 were 161.4 F g^{-1}, 166.3 F g^{-1}, 97.3 F g^{-1}, 114 F g^{-1} and 91.8 F g^{-1}, respectively (Fig. 2c, d). To make a clear contrast with previous studies, we listed the most similar literatures available (Table S3, Supporting Information) about the production of layer capacitor materials using active carbon. Although they used different methods with our study, but the mechanisms of these methods were compatible. Results showed that the capacitance of the EDLC materials we achieved was higher than those produced using traditional methods. Since the best capacity performance was obtained under the conditions of 100 mg L^{-1} and 600 °C, the control was produced from biochar without adsorbing Ni^{2+} and named as BC6-K6. The high concentration of nickel might lead to more large particles on the carbon surface and as a result, some of the pore structures were unable to provide electrochemical adsorption sites for the ions in electrolyte [35], so the double-layer capacitance of the carbon materials decreased heavily from BC6-Ni1-K6 to BC6-Ni5-K6.

The CV curves (Fig. 2a, b) showed that the materials had similar capacitive properties to activated carbon and there were also many small pseudo-capacitive reaction peaks. The reduction peak of metallic nickel was observed at −0.76 V and −0.72 V for BC6-Ni1-K8 and BC6-Ni5-K8, respectively, which could possibly be attributed to the formation of graphite structure at the activation temperature of 800 °C, as proved by XRD patterns (Fig. S1a). For the activation temperature of 600 °C and 700 °C, fewer functional groups can be found on the surface of carbon layer (Fig. S1b), and could be detected by the CV curves at the potential range of −0.2 ~ −0.15 V and −0.92 V. Those faradic redox reaction peaks at −0.92 V and −0.2 V could be seen more clearly in the control group of BC6-K6 in Fig. 3a. Meanwhile Fig. 3a mainly indicated that the presence of nickel could promote the electrochemical capacity at the activation temperature of 600 °C.

Based on the above results, the EDLC material with the best capacitive performance, BC6-Ni1-K6, was chosen to conduct further electrochemical characterization that compared with its control, BC6-K6 (Fig. 3). It's shown that BC6-Ni1-K6 had a higher capacitance than the control, BC6-K6, observed from the larger area of CV curve for BC6-Ni1-K6 in Fig. 3a. A good reversibility was observed from the current

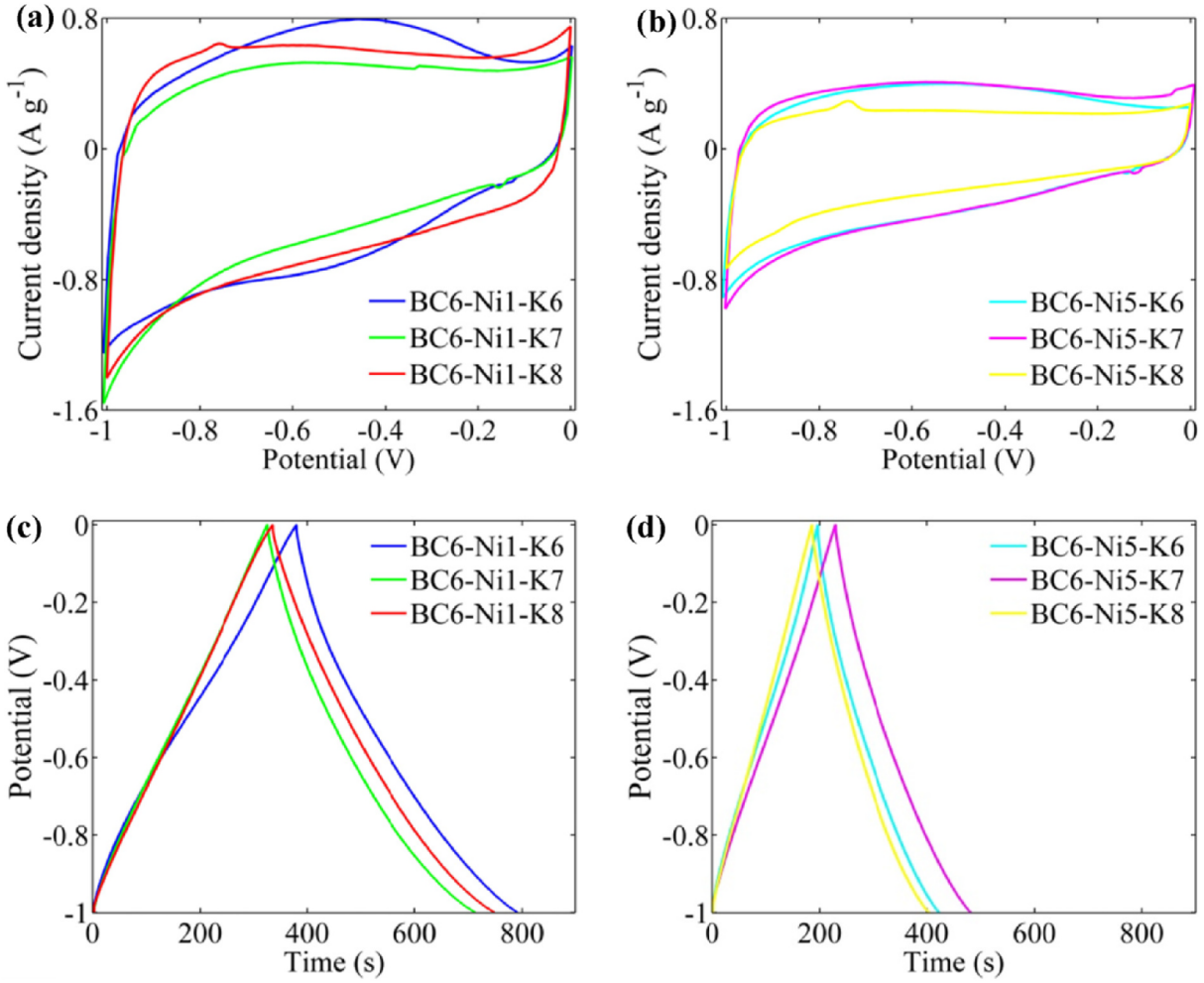

Fig. 2. Electrochemical performances of EDLC materials with different Ni^{2+} concentrations and activation temperatures, measured in a three-electrode system with Hg\HgO as reference electrode. (a) CV curves for EDLC materials at 5 mV s^{-1} in the potential window of $-1 \sim 0$ V. (b) GCD curves at the current density of 0.5 A g^{-1}.

density at different scanning rates from 5 mV s^{-1} to 100 mV s^{-1}, which suggested that this material can be used at high current density conditions (Fig. 3b). Compared with the control without Ni embedded (BC6-K6, 98.4 F g^{-1}), BC6-Ni1-K6 showed a much higher capacitance of 188.9 F g^{-1} at 0.5 A g^{-1} (Fig. 3c) revealing the potential of Ni to enhance the capacitive performance. As shown in Fig. 3d, the capacity performance of BC6-Ni1-K6 was much higher than BC6-K6 at different current densities from 0.5 to 10 A g^{-1}, and the capacitances of BC6-Ni1-K6 and BC6-K6 at 10 A g^{-1} were 124 F g^{-1} and 84 F g^{-1}, respectively. Compared with BC6-K6, the enhanced capacitance for BC6-Ni1-K6 might be attributed to the enlarged mesoporous structure. After 1000 cycles, although both BC6-Ni1-K6 and BC6-K6 could keep their capacity above 95.6% at 10 A g^{-1}, according to Fig. 3e, BC6-Ni1-K6 always showed a much higher capacitive performance than BC6-K6.

The impedance spectrum (Fig. 3f) was conducted for BC6-Ni1-K6 and BC6-K6 to characterize the resistance in the circuit, the capacitance for carbon materials and the diffusion resistance of ions between the electrolyte and carbon surface [36]. There were three parts in EIS spectrum including a semicircle in the high frequency region, a slope angle about 45° in the mediate, and a straight line almost perpendicular to X-axis in the low frequency region. From the original EIS data, equivalent series resistance (ESR) for BC6-Ni1-K6 (2.02 Ω) and BC6-K6 (2.27 Ω) were calculated from the X-intercept of Nyquist spectrum at high frequency region, which took the resistance of electrolyte, carbon materials and the interconnection between current collector and active materials into consideration [37]. The charge transfer resistance (Rct) and Warburg impedance (W) were estimated with the circuit model of R(C(RW)) (C) [38,39]. Fig. 3f showed that at the high frequency region, the semicircle diameter of BC6-Ni1-K6 was larger than BC6-K6, indicating that BC6-Ni1-K6 (Rct = 0.63 Ω, mass loading = 5.17 mg) has a high charge transfer resistance than BC6-K6 (Rct = 0.44 Ω, mass loading = 3.09 mg). However, after the normalization of unit mass, it was found that the index (Rct/mass) of BC6-Ni1-K6 was smaller than BC6-K6 (Table 1), which confirmed the difference in capacitance performance. The transition part in the middle of EIS curves reflected the Warburg impedance of the materials [40]. The results showed that the ionic diffusion resistance of BC6-Ni1-K6 (0.596 Ω $s^{-1/2}$) was lower than that of BC6-K6 (0.757 Ω $s^{-1/2}$), indicating that it had abundant mesoporous structure. As shown in Table 1, all the impedance indexes of BC6-Ni1-K6 were smaller than BC6-K6, which further confirmed that the adsorption of Ni^{2+} had potential to promote capacitance performance.

3.2. Presence of nickel facilitated the decomposition of carbonate

In order to probe the crystal structure of the products and explore the major chemical reactions that occurred during the activation process of the recycled nickel-laden biochar, XRD analysis was conducted and patterns could be seen in Fig. 4a. For the control sample without nickel (BC6-K6), there were two peaks detected at 32.7° and 29.4°, representing magnesium carbonate ($MgCO_3$) and calcium carbonate ($CaCO_3$) respectively, which were identified in Fig. S2 (Supporting

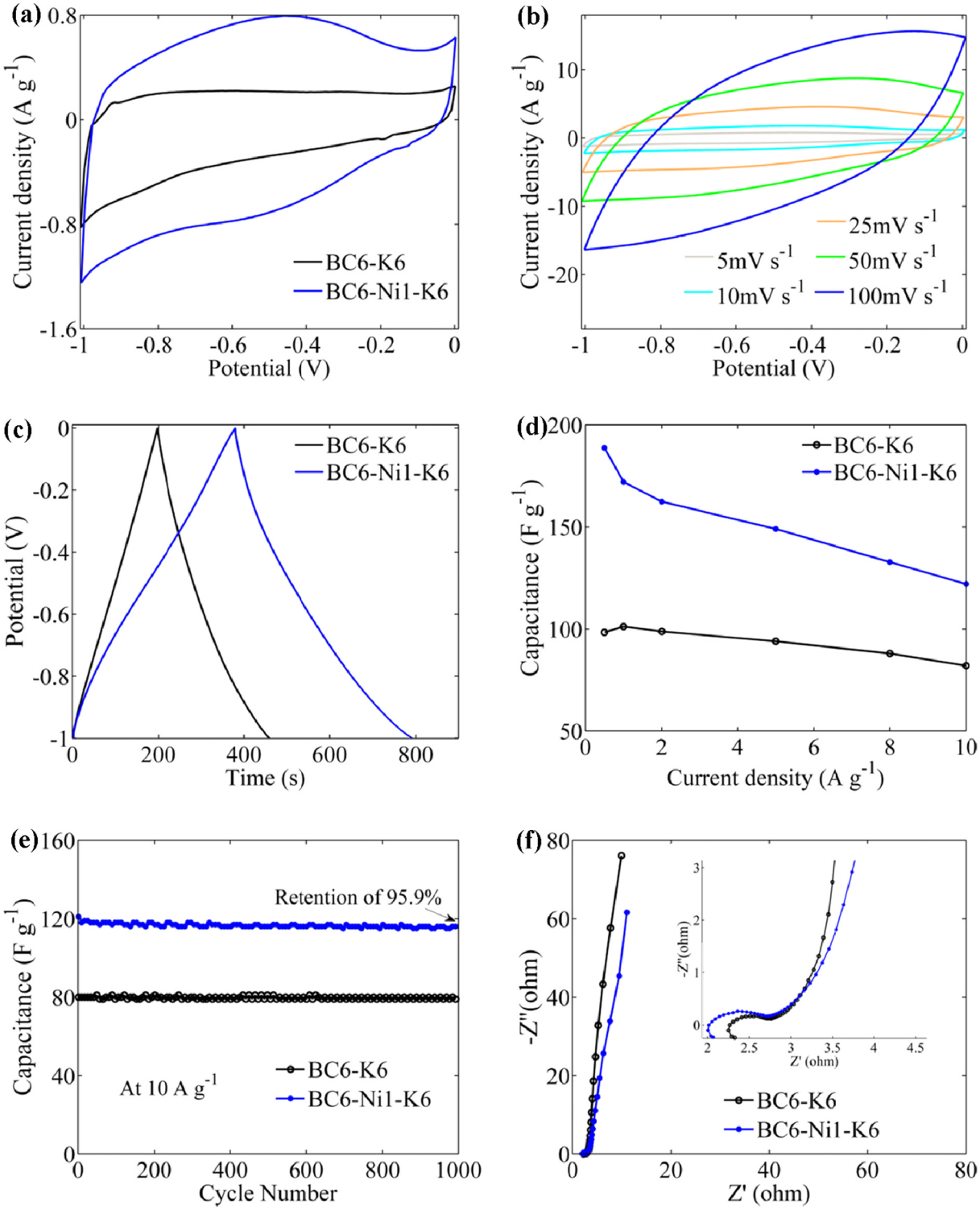

Fig. 3. The electrochemical performances of BC6-K6 and BC6-Ni1-K6 tested at three electrode system with the reference electrode of Hg\HgO. (a) CV curves at 5 mV s^{-1} in the potential window of $-1 \sim 0$ V. (b) CV curves for BC6-Ni1-K6 at different scan rate from 5 mV s^{-1} to 100 mV s^{-1}. (c) GCD curves at the current density of 0.5 A g^{-1}. (d) Specific capacitance performance at different current density from 0.5 ~ 10 A g^{-1}. (e) Cycling stability at the current density of 10 A g^{-1}. (f) Nyquist plot measured from 0.01 Hz to 10 kHz at 5 mV.

Table 1
Electrochemical property measured from Nyquist spectrum.

Samples	Mass load (mg)	ESR (Ω)/mg	Rct (Ω)/mg	W (Ω $s^{-1/2}$)/mg
BC6-K6	3.09	2.27/3.09 = 0.73	0.44/3.09 = 0.14	0.757/3.09 = 0.24
BC6-Ni1-K6	5.17	2.02/5.17 = 0.39	0.63/5.17 = 0.12	0.596/5.17 = 0.12

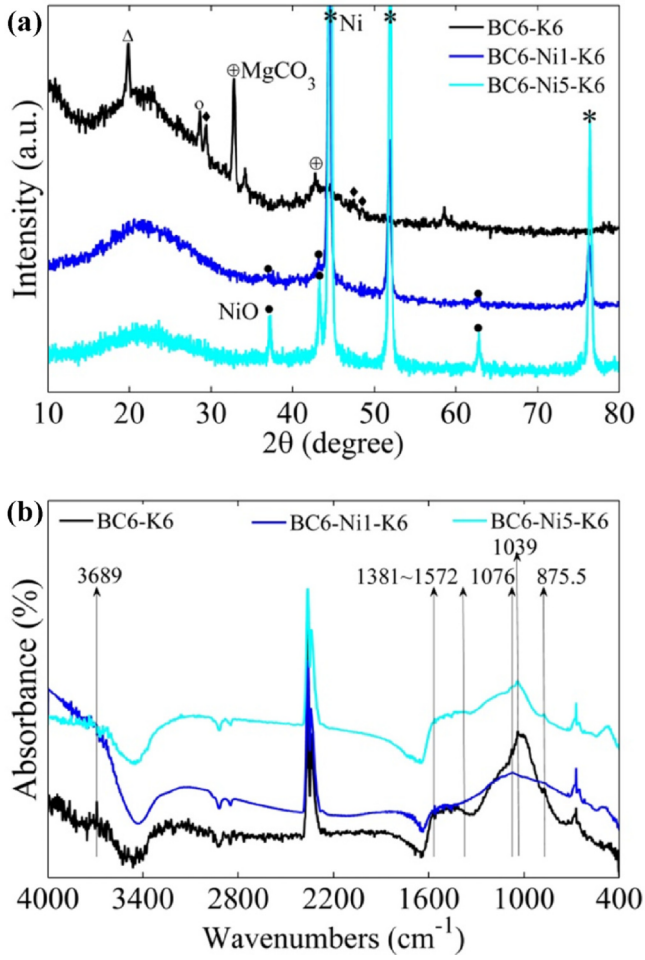

Fig. 4. The XRD patterns (a) and FTIR spectra (b) for EDLC materials.

Information). Substantial presence of carbonate in BC6-K6 suggested that the decomposition of carbonate and transformation into metal oxide and CO_2 haven't finished at 600 °C. This consists with the results shown in Maitra's research [41]. Peaks for metallic nickel and nickel oxide were observed in XRD spectrum for BC6-Ni1-K6 and BC6-Ni5-K6 in Fig. 4a, while carbonate peaks disappeared. It indicated that the presence of nickel facilitated the decomposition of carbonates and accelerated their collapse, and similar catalytic effect has been reported for the performance of Co [14]. The reactions in Table S4 could explain this phenomenon and the participation of nickel in the KOH activation process could be figured out in Eqs. (2–6) [42–44].

$$NiO + H_2 \rightarrow Ni + H_2O\uparrow \quad (2)$$

$$NiO + C \rightarrow Ni + CO\uparrow \quad (3)$$

$$2NiO + C \rightarrow 2Ni + CO_2\uparrow \quad (4)$$

$$NiO + CO \rightarrow Ni + CO_2\uparrow \quad (5)$$

$$Ni + 2KOH \rightarrow NiO + K_2O + H_2\uparrow \quad (6)$$

At the same time, the decomposition of carbonates reacted at a slow rate (Eq. (7–9)), where the CO_2 produced in this process was slowly blown away [41,45].

$$CaCO_3 \rightarrow CaO + CO_2\uparrow \quad (7)$$

$$MgCO_3 \rightarrow MgO + CO_2\uparrow \quad (8)$$

$$K_2CO_3 \rightarrow K_2O + CO_2\uparrow \quad (9)$$

During the pyrolysis process, the reduction of nickel oxide was dominant that accelerated the formation of hydrogen as shown in Eq. (6), making it easier to reduce metal oxides of alkali [44,46].

$$H_2 + K_2O \rightarrow H_2O\uparrow + 2K \quad (10)$$

Although the amount of hydrogen is limited in this system, but under the reduction condition, once the nickel oxide was produced, it tended to be reduced to metallic nickel (Eq. (2–5)). The metallic nickel would further accelerate the decomposition of KOH (Eq. (6)) and carbonate. The peaks of nickel oxide in Fig. 4a proved the mechanism and Fig. 7a showed the process directly (nickel eroded the carbon particle). Accompanied with the KOH activation, the decomposition of carbonates (K_2CO_3, $MgCO_3$ and $CaCO_3$) generated metallic alkali metals which acted as etching agent to strengthen the pores expansion in carbon matrix [46]. It can be inferred that the presence of nickel affected the overall pore structure of the materials indirectly.

This catalytic effect of Ni at different concentrations could not be verified from the XRD patterns, but combined with the electrochemical properties of the materials, it could be preliminarily speculated that the etching effect of metallic potassium is more obvious at low nickel concentration than high concentration, which can be attributed to the formation of larger particles of metallic nickel crystal structure under higher concentration. The crystal size of metallic nickel formed at different Ni^{2+} concentrations could be calculated by constant full width at half maximum (FWHM), and it was found that the crystal size of nickel particles formed at the concentration of 100 mg g^{-1} (23.6 nm) was smaller than 500 mg g^{-1} (32.4 nm).

Fig. S1a (Supporting Information) showed the XRD patterns for samples produced at different activation temperatures (600 °C, 700 °C and 800 °C), and a small peak of diopside (2θ = 29.8°) was detected for BC6-Ni1-K7; The graphite structure (2θ = 26.46°) was observed for BC6-Ni1-K8 which can be attributed to the catalysis of Ni like the effect of Fe [47]. The previous study of KOH activation had shown that metallic potassium appeared around 700 °C [46], thus compared with BC6-Ni1-K6, all of the NiO would transferred to Ni at this reduction atmosphere for BC6-Ni1-K7 and BC6-Ni1-K8. According to the calculation based on the constant FWHM, the average size of nickel particles increased with treatment temperature, i.e., the values were 23.6 nm, 28.4 nm and 29.9 nm for BC6-Ni1-K6, BC6-Ni1-K7 and BC6-Ni1-K8 respectively. At high temperatures, the catalytic reaction quickly accomplished and the size of nickel particles grew and blocked the pore structure on the surface of the carbon layer, which was disadvantageous to the capacitive properties [35]. Therefore, the sample produced at 600 °C activation temperature showed a better electrochemical property than the sample treated with 700 °C and 800 °C, which was due to that the average size of nickel particles formed at higher temperature was larger than those formed at lower temperature, and they covered the surface of biochar occupying part of the adsorption sites for positive ions.

In this study, the presence of Ni further catalyzed the degradation of organic matter, and accelerated the decomposition of the surface functional groups. Almost no difference could be observed between the surface functional groups of the capacitive material prepared at 600 °C and those at 700 °C and 800 °C (Fig. S1b). Fig. 4b showed the FTIR spectrum of BC6-K6, BC6-Ni1-K6 and BC6-Ni5-K6. Compared with the control, BC6-K6, the vibration peaks between 1381 cm^{-1} and 1572 cm^{-1} were slightly weaker for BC6-Ni1-K6 and BC6-Ni5-K6, which indicates that metallic Ni could promote the formation of aromatic structures and reduce the carbon with sp^3 hybridization [48]. The peaks at 1076 cm^{-1} and 1039 cm^{-1} representing the vibration of carbon–oxygen bond and alcohol hydroxyl respectively [49,50], were both higher for BC6-K6 than those of samples with Ni in it, which can be seen from Fig. 4b and Fig. S1b (Supporting Information). The alcohol hydroxyl peaks at 1039 cm^{-1} disappeared in BC6-Ni1-K6, but remained in BC6-Ni5-K6. In addition, different from BC6-K6, the peaks at 875.5 cm^{-1} for external bending vibration of C–H in BC6-Ni1-K6 became weaker conforming that the nickel has a huge effect on the carbon surface [51].

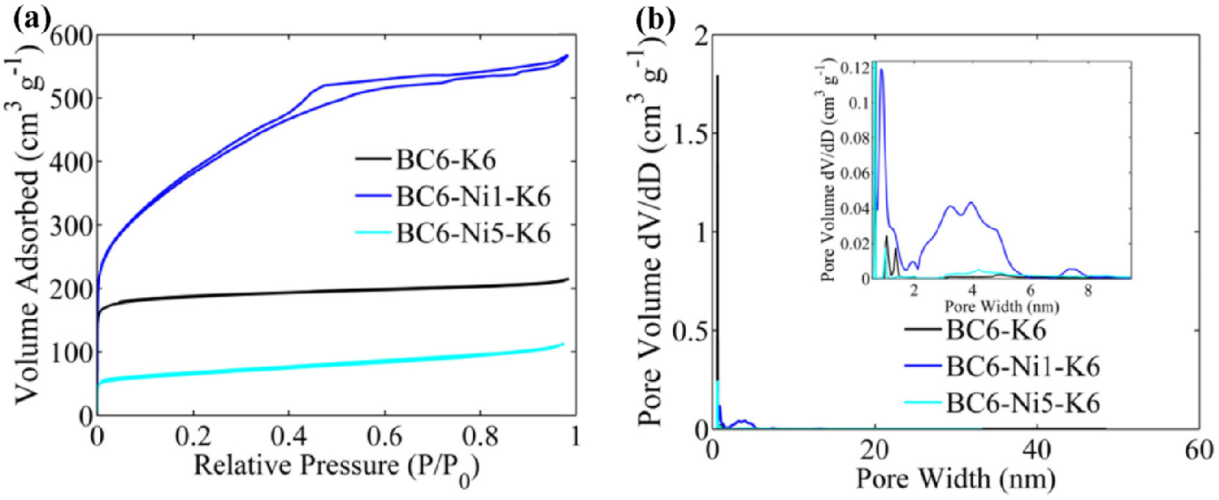

Fig. 5. BET test for BC6-K6, BC6-Ni1-K6 and BC6-Ni5-K6. (a) Nitrogen adsorption–desorption isothermals. (b) The pore size distribution curves.

3.3. Nickel contributed to the erosion of carbon layer

The surface areas of the EDLC materials based on the BET measurement were presented in Fig. 5. Nitrogen adsorption–desorption isothermals curves showed that BC6-Ni1-K6 had the highest N_2 adsorption performance with the surface area of 1181 $m^2\ g^{-1}$ and pore volume of 0.81 $cm^3\ g^{-1}$. Meanwhile, the specific surface area of BC6-K6 and BC6-Ni5-K6 were only 805.9 $m^2\ g^{-1}$ and 259.3 $m^2\ g^{-1}$ respectively (Fig. 5a). Since there was a vertical line at low pressure region, the initial adsorption occurred firstly in micro-pores and then the curves for BC6-K6 and BC6-Ni5-K6 with fewer mesoporous getting flat, while the curves for BC6-Ni1-K6 continued to increase significantly (Fig. 5a). The pore size distribution curves in Fig. 5b indicated that BC6-Ni1-K6 contained a large amount of mesoporous structures (2 ~ 6 nm) and a small amount of microporous structures (< 2 nm), since the graphitization process prevented the formation of microporous structure [27]. In contrast, BC6-K6 had plenty of microporous structures, which performed like the typical activated carbon. The BET data in Table 2 further confirmed that BC6-K6 contained mainly microporous structure (87% Volume, 98% surface area), while BC6-Ni1-K6 was predominantly mesoporous (67% Volume, 47% surface area) and for BC6-Ni5-K6, it lacked both micropores and mesopores.

The pore structure of BC6-Ni1-K6 could be further observed through SEM from RISE in Fig. 6. There were some macro-porous structures in the EDLC material, large amounts of fine nano-crystalline nickel particles dispersed on the surface and inside the macro-pores of the material. Since the diameter of nickel particles was widely distributed and the XRD results show that the average particle size of metallic nickel was about 23.6 nm from constant FWHM, it was inferred that there must be plentiful nanoparticles nickel in the carbon matrix. Meanwhile, it could also be observed that nickel particles tend to invade into carbon layer (Fig. 6b). And Fig. 6c showed that large amounts of nanoparticles aggregated at porous channel, which can further assist the formation of mesoporous structure of the material. As also could be seen from Fig. S3a and b (Supporting Information), most of the nickel particles were fixed on the surface of carbon materials, and tended to fuse with carbon materials.

The EDS from RISE was used to characterize the elements distribution on the carbon surface to explore the chemical reactions during pyrolysis. Fig. 7 exhibited the main elements distribution including carbon, nickel and oxygen. After KOH activation, washing the products with deionized water could retain most of the original reaction information and fixed the waste metallic nickel on carbon layer effectively while the traditional KOH activation use acid to wash the products. But at the same time, deionized water did not sufficiently clean the alkali metals like potassium and magnesium in Fig. 7a. As can be seen from Fig. 7b, the main component of the white small particles in SEM images was nickel, and the particles also contained oxygen, indicating the presence of nickel oxide, which further proved the catalytic reaction. The distribution of carbon and nickel element showed that the carbon content in the large nickel particles was relatively low, while there was no difference among the small nickel particles. Those phenomena indicated that the metallic nickel and nickel oxide can react with the carbon material during the KOH activation process and gradually fuse with carbon.

How nickel participated in the KOH activation process? Firstly, KOH activation involves dehydration, production of hydrogen and carbon monoxide [52], as well as the etching of carbon layer by metallic potassium [46]. The metallic potassium in the activated carbon material could be easily rinsed by acid in traditional KOH activation method, so it would not adversely affect the properties of the products. The main reactions occurred in KOH activation were expressed as follows [45,53]

$$H_2O(s) \rightarrow H_2O(g) \quad \sim 200\ ^oC - 300\ ^oC \tag{11}$$

$$2KOH \rightarrow K_2O + H_2O \quad \sim 400\ ^oC \tag{12}$$

$$C + H_2O \rightarrow CO + H_2 \quad \geqslant 500\ ^oC \tag{13}$$

$$CO + H_2O \rightarrow CO_2 + H_2 \quad \sim 500\ ^oC \tag{14}$$

$$CO_2 + K_2O \Leftrightarrow K_2CO_3 \tag{15}$$

K_2O is formed from the dehydration of KOH, after initial dehydration at low and medium temperature. At about 500 ˚C, carbon starts to react with water vapor to produce H_2 and CO, and then CO further transforms to CO_2 through reaction with H_2O. Besides, CO_2 is easy to

Table 2
Pore structure characterization from BET.

Samples	BET Surface Area $m^2\ g^{-1}$	Micro-pore/Mesoporous Surface Area ($m^2\ g^{-1}$)	Pore Volume ($cm^3\ g^{-1}$)	Micro-pore/Mesoporous Volume ($cm^3\ g^{-1}$)
BC6-K6	805.9	787.2/18.7	0.30	0.26/0.04
BC6-Ni1-K6	1181.1	629.3/551.8	0.81	0.27/0.54
BC6-Ni5-K6	259.3	203.3/56.0	0.16	0.07/0.09

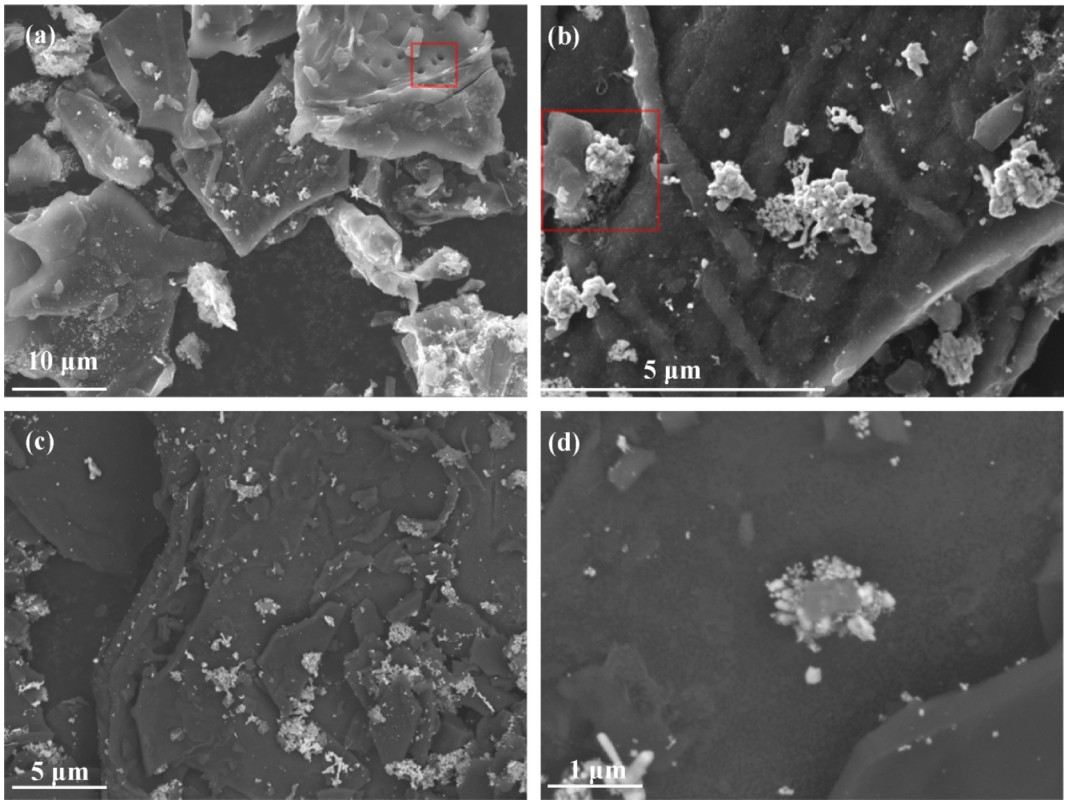

Fig. 6. SEM images of the samples from biochar adsorbing 100 mg L^{-1} Ni^{2+} and activated at 600 °C (BC6-Ni1-K6). (a) and (b) represent the position one with the scale of 10 μm and 5 μm. (c) and (d) represent another position with the scale of 5 μm and 1 μm.

react with K_2O to form K_2CO_3. After that, K_2CO_3 can be converted into metallic potassium and CO at around 700 °C in the normal KOH activation process, and it would be transformed completely at 800 °C [17]. The main reactions over 700 °C include:

$$K_2CO_3 \rightarrow K_2O + CO_2 \quad (16)$$

$$CO_2 + C \rightarrow CO \quad (17)$$

$$C + K_2O \rightarrow 2K + CO \quad (18)$$

$$K_2CO_3 + 2C \rightarrow 2K + 2CO \quad (19)$$

With the participation of nickel, hydrogen and CO could reduce the nickel oxide to metallic nickel at the carbon surface, since the nickel particles 'stood' there in Fig. 6d. The reduction process of nickel has been discussed at the catalyst reactions in part 2 (Eq. (2–5)). Nickel hydroxide was firstly dehydrated to produce nickel oxide, and since hydrogen had the strongest reduction capacity, a part of nickel oxide was then reduced by hydrogen. The metallic nickel produced would accelerate the decomposition of KOH to produce more hydrogen and metallic potassium [44], thus led to the reduction of alkali metal oxides (Eq. (10)). At the same time, CO and carbon would react with nickel oxide to produce metallic nickel, and the nickel particles would gradually invade into the carbon layer shown in Fig. 6b since the nickel oxide is more likely to react with volatiles which has more sp^3 hybridized carbon [51,54].

3.4. Nickel promoted the formation of aromatic hydrocarbon structure

In order to further explore the erosion of nickel on carbon materials, the in situ Raman spectroscope from RISE for BC6-Ni1-K6 was carried out, and the results were shown in Fig. 8. In Fig. 8a, the green part represented the carbon in more sp^3 hybridization, in which the D peak was stronger than G peak; the blue district was designated as more sp^2 hybridization area with the G peak being higher than D peak; the red and yellow parts were fluorescence interference regions, and the blue region in the lower right corner was mainly caused by the fact that carbon layers were not in the same plane as the SEM shown. It could be seen from Fig. 8a that the G peak was significantly higher than the D peak near the nickel particles, which indicated that sp^2 hybridized carbon was more likely to be near the metallic nickel, while more sp^3 hybridized carbon located near the area without nickel. This was consistent with the conclusion that metallic iron promoted the formation of aromatic carbon as a catalyst [47]. Another possibility was that in the reduction process of nickel oxide, sp^3 hybridized carbon was more readily decomposed to CO or CO_2 and lost as gas, while sp^2 aromatic carbon was more stable and retained in the solid phase [54]. Combined with Fig. 6a, it could be seen from the optical microscope diagram of Fig. 8b that the large nickel particles were still shown in white. The measurement area for Raman was conducted on a relatively flat plane, with some large nickel particles and some scattered small particles distributed on the platform. In order to reflect the Raman test more intuitively, three points were selected for further exploration. The difference between the D peak and the G peak in the vicinity of nickel particles could be seen more clearly in Fig. 8c. Moreover, G' peaks were observed from where it is located in the area adjacent to nickel particles, which further indicated that the carbon near nickel particles tended to be form sp^2 hybrid aromatic hydrocarbon structure.

Therefore, in the process of preparing EDLC materials from biochar after adsorbing Ni^{2+} from wastewater, if the Ni^{2+} were dispersed evenly and the pyrolysis temperature was controlled precisely, nickel-carbon materials with more mesoporous structures could be obtained by KOH activation. The mesoporous structure was mainly formed via the catalytic effect of Ni, which consumed a large amount of carbon. Nickel could simultaneously promote the carbonate decomposition and further affect the KOH activation process, as well as assist the formation of more sp^2 hybrid aromatic carbon.

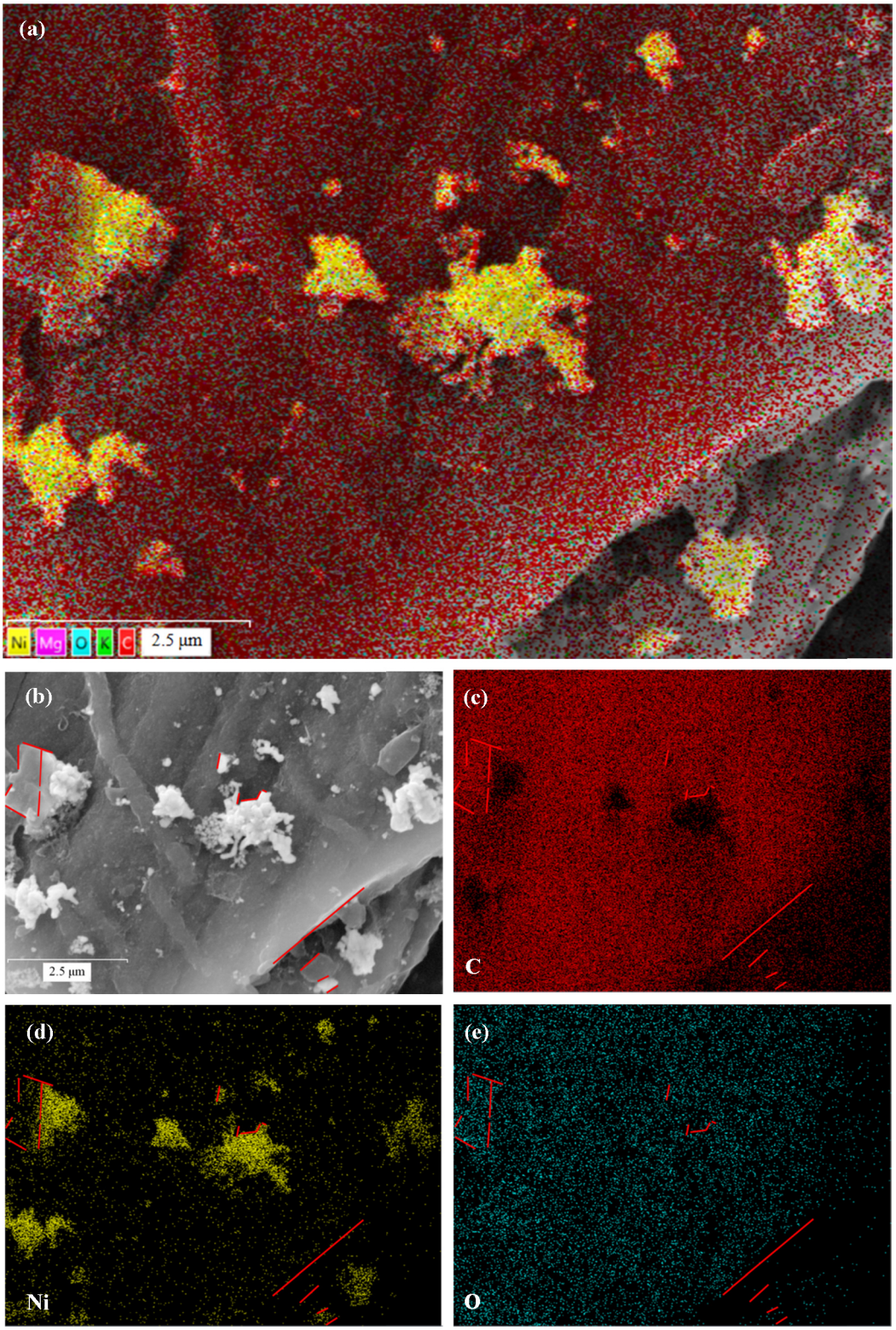

Fig. 7. The EDS of BC6-Ni1-K6 measured by RISE. (a) Layered image combined the distribution of Ni, Mg, O, K, C and its original SEM. (b) The scanning area for EDS. (c), (d) and (e) indicate the distribution of C, Ni and O.

4. Conclusions

The reclamation of exhausted biochar after adsorbing Ni^{2+} from wastewater to produce EDLC materials was performed. Compared with the control without adsorbing nickel, the biochar laden with nickel showed a capacitive performance of 188.9F g^{-1}, while the control was only 98.4F g^{-1}. In addition, the biochar adsorbing a lower concentration (100 mgNi^{2+} g^{-1}) of nickel achieved the higher capacitive performance than the high concentration (500 mgNi^{2+} g^{-1}). The relatively lower activation temperature as 600 °C was more preferred in contrast of higher temperature as more than 700 °C in achieving better capacitive performance.

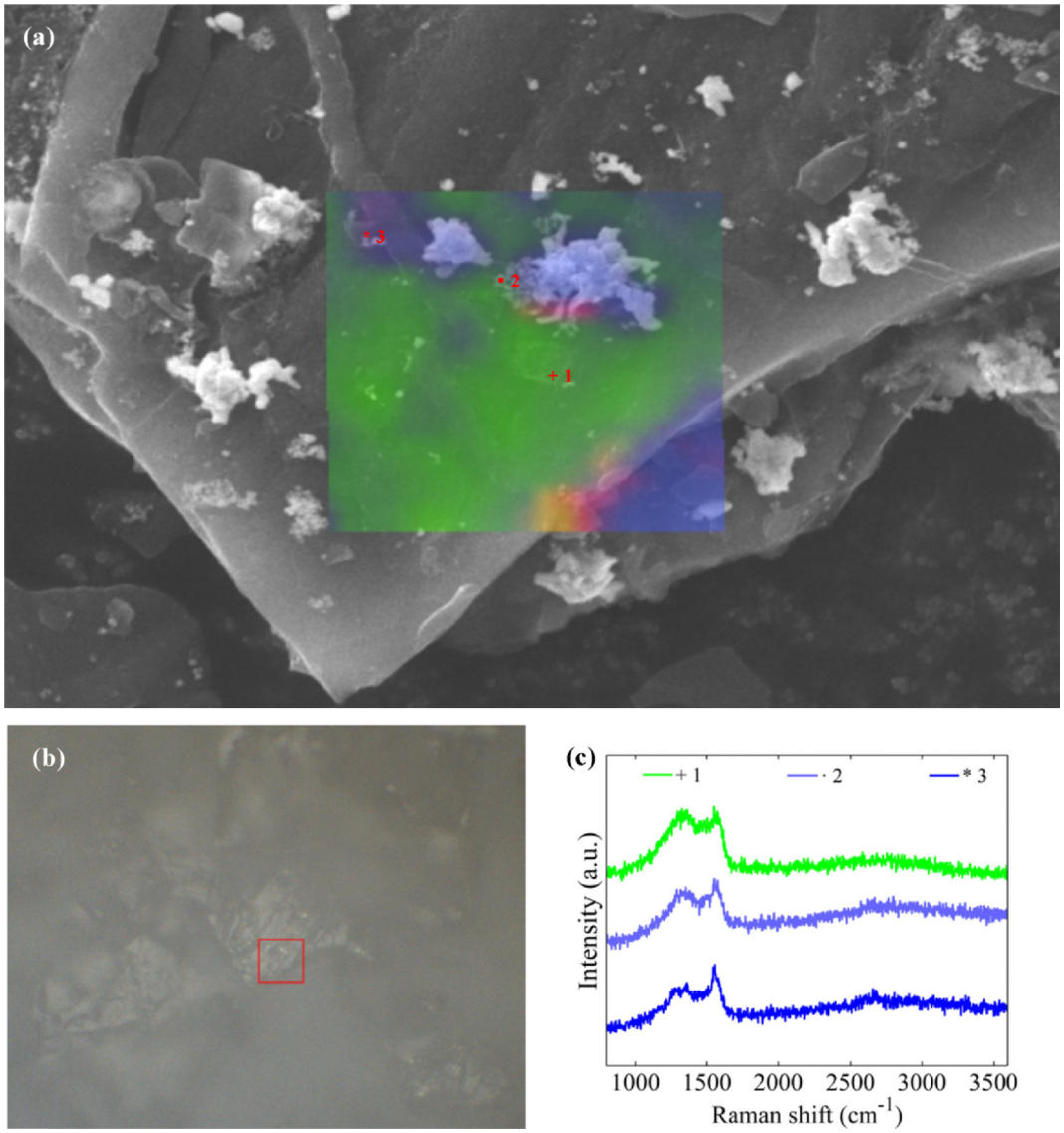

Fig. 8. In situ Raman spectrum of BC6-Ni1-K6 combined with SEM from RISE. (a) The combination of SEM and in situ Raman with area scanning. (b) Optical microscope diagram of the selected area. (c) Three typical points in the selected area.

From the characterization results, it was speculated that the formation of mesoporous structure in this material dominated the performance of the capacitance. Mechanism exploration by means of instruments confirmed that presence of nickel facilitated the decomposition of carbonates inducing more production of metallic elements for creating pores. Meanwhile, with the presence of moderate concentration of nickel, the erosion of carbon layer and formation of aromatic hydrocarbon structure were both accelerated. This study provides a feasible and simple strategy of reclaiming waste biochar after adsorbing heavy metals to prepare capacitive material.

Declaration of Competing Interest

The authors declare that they have no known competing financial interests or personal relationships that could have appeared to influence the work reported in this paper.

Acknowledgements

We appreciate the support from National Natural Science Foundation of China (No. 41877110).

Appendix A. Supplementary data

Supplementary data to this article can be found online at https://doi.org/10.1016/j.cej.2020.126856.

References

[1] Y. Xue, B. Gao, Y. Yao, M. Inyang, M. Zhang, A. Zimmerman, K. Ro, Hydrogen peroxide modification enhances the ability of biochar (hydrochar) produced from hydrothermal carbonization of peanut hull to remove aqueous heavy metals: Batch and column tests, Chem. Eng. J. 200–202 (2012) 673–680.
[2] L. Wang, Y. Wang, F. Ma, V. Tankpa, S. Bai, X. Guo, X. Wang, Mechanisms and reutilization of modified biochar used for removal of heavy metals from wastewater: A review, Sci. Total Environ. 668 (2019) 1298–1309.
[3] M. Uchimiya, S. Chang, K.T. Klasson, Screening biochars for heavy metal retention in soil: role of oxygen functional groups, J. Hazard. Mater. 190 (2011) 432–441.
[4] H. Lu, W. Zhang, Y. Yang, X. Huang, S. Wang, R. Qiu, Relative distribution of Pb^{2+} sorption mechanisms by sludge-derived biochar, Water Res. 46 (2012) 854–862.
[5] S.K. Poonam, N. Bharti, Kumar, Kinetic study of lead (Pb^{2+}) removal from battery manufacturing wastewater using bagasse biochar as biosorbent, Appl. Water Sci. 8 (2018) 1–13.
[6] A.A. Alqadami, M.A. Khan, M. Otero, M.R. Siddiqui, B.-H. Jeon, K.M. Batoo, A magnetic nanocomposite produced from camel bones for an efficient adsorption of toxic metals from water, J. Clean. Prod. 178 (2018) 293–304.
[7] C. Gan, Y. Liu, X. Tan, S. Wang, G. Zeng, B. Zheng, T. Li, Z. Jiang, W. Liu, Effect of porous zinc-biochar nanocomposites on Cr(VI) adsorption from aqueous solution,

RSC Adv. 5 (2015) 35107–35115.
[8] Y. Ding, Y. Liu, S. Liu, Z. Li, X. Tan, X. Huang, G. Zeng, Y. Zhou, B. Zheng, X. Cai, Competitive removal of Cd(II) and Pb(II) by biochars produced from water hyacinths: performance and mechanism, RSC Adv. 6 (2016) 5223–5232.
[9] Y. Wang, Y. Zhang, L. Pei, D. Ying, X. Xu, L. Zhao, J. Jia, X. Cao, Converting Ni-loaded biochars into supercapacitors: Implication on the reuse of exhausted carbonaceous sorbents, Sci. Rep. 7 (2017) 41523.
[10] A.C. Nwanya, M.M. Ndipingwi, N. Mayedwa, L.C. Razanamahandry, C.O. Ikpo, T. Waryo, S.K.O. Ntwampe, E. Malenga, E. Fosso-Kankeu, F.I. Ezema, E.I. Iwuoha, M. Maaza, Maize (Zea mays L.) fresh husk mediated biosynthesis of copper oxides: Potentials for pseudo capacitive energy storage, Electrochim. Acta 301 (2019) 436–448.
[11] P. Hao, X. Ma, J. Xie, F. Lei, L. Li, W. Zhu, X. Cheng, G. Cui, B. Tang, Removal of toxic metal ions using chitosan coated carbon nanotube composites for supercapacitors, Sci. China Chem. 61 (2018) 797–805.
[12] C.L. Burket, R. Rajagopalan, H.C. Foley, Synthesis of nanoporous carbon with pregraphitic domains, Carbon 45 (2007) 2307–2310.
[13] A.K. Raj, M.R. Panda, D.P. Dutta, S. Mitra, Bio-derived mesoporous disordered carbon: An excellent anode in sodium-ion battery and full-cell lab prototype, Carbon 143 (2019) 402–412.
[14] S. Yang, S. Wang, X. Liu, L. Li, Biomass derived interconnected hierarchical micro-meso-macro- porous carbon with ultrahigh capacitance for supercapacitors, Carbon 147 (2019) 540–549.
[15] M. Song, Y. Zhou, X. Ren, J. Wan, Y. Du, G. Wu, F. Ma, Biowaste-based porous carbon for supercapacitor: The influence of preparation processes on structure and performance, J. Colloid Interface Sci. 535 (2019) 276–286.
[16] C. Zhao, J. Li, W. Chen, Y. Yang, K. Chiang, N. Burke, Synthesis and electrochemical properties of ordered mesoporous carbon supported well-dispersed cobalt oxide nanoparticles for supercapacitor, Mater. Res. Bull. 64 (2015) 55–60.
[17] J. Wang, S. Kaskel, KOH activation of carbon-based materials for energy storage, J. Mater. Chem. 22 (2012) 23710–23725.
[18] S. Ghosh, R. Santhosh, S. Jeniffer, V. Raghavan, G. Jacob, K. Nanaji, P. Kollu, S.K. Jeong, A.N. Grace, Natural biomass derived hard carbon and activated carbons as electrochemical supercapacitor electrodes, Sci. Rep. 9 (2019) 16315.
[19] Q. Li, R. Jiang, Y. Dou, Z. Wu, T. Huang, D. Feng, J. Yang, A. Yu, D. Zhao, Synthesis of mesoporous carbon spheres with a hierarchical pore structure for the electrochemical double-layer capacitor, Carbon 49 (2011) 1248–1257.
[20] D.M. Mijailović, M.M. Vukčević, Z.M. Stević, A.M. Kalijadis, D.B. Stojanović, V.V. Panić, P.S. Uskoković, Supercapacitive performances of activated highly microporous natural carbon macrofibers, J. Electrochem. Soc. 164 (2017) A1061–A1068.
[21] D. Saha, Y. Li, Z. Bi, J. Chen, J.K. Keum, D.K. Hensley, H.A. Grappe, H.M. Meyer, S. Dai, M.P. Paranthaman, A.K. Naskar, Studies on supercapacitor electrode material from activated lignin-derived mesoporous carbon, Langmuir 30 (2014) 900–910.
[22] T. Purkait, G. Singh, M. Singh, D. Kumar, R.S. Dey, Large area few-layer graphene with scalable preparation from waste biomass for high-performance supercapacitor, Sci. Rep. 7 (2017) 15239.
[23] S.T. Neeli, H. Ramsurn, Synthesis and formation mechanism of iron nanoparticles in graphitized carbon matrices using biochar from biomass model compounds as a support, Carbon 134 (2018) 480–490.
[24] A. Trubetskaya, G. Surup, A. Shapiro, R.B. Bates, Modeling the influence of potassium content and heating rate on biomass pyrolysis, Appl. Energy 194 (2017) 199–211.
[25] X.-Q. Liu, H.-S. Ding, Y.-Y. Wang, W.-J. Liu, H. Jiang, Pyrolytic temperature dependent and ash catalyzed formation of sludge char with ultra-high adsorption to 1-naphthol, Environ. Sci. Tech. 50 (2016) 2602–2609.
[26] W.D. Chanaka Udayanga, A. Veksha, A. Giannis, G. Lisak, T.-T. Lim, Effects of sewage sludge organic and inorganic constituents on the properties of pyrolysis products, Energy Convers. Manag. 196 (2019) 1410–1419.
[27] M. Sevilla, A.B. Fuertes, Fabrication of porous carbon monoliths with a graphitic framework, Carbon 56 (2013) 155–166.
[28] L. Jiang, J. Yan, L. Hao, R. Xue, G. Sun, B. Yi, High rate performance activated carbons prepared from ginkgo shells for electrochemical supercapacitors, Carbon 56 (2013) 146–154.
[29] M. Inagaki, M. Toyoda, Y. Soneda, S. Tsujimura, T. Morishita, Templated mesoporous carbons: Synthesis and applications, Carbon 107 (2016) 448–473.
[30] T. Mehtab, G. Yasin, M. Arif, M. Shakeel, R.M. Korai, M. Nadeem, N. Muhammad, X. Lu, Metal-organic frameworks for energy storage devices: Batteries and supercapacitors, J. Energy Storage 21 (2019) 632–646.
[31] B. Liu, H. Shioyama, H. Jiang, X. Zhang, Q. Xu, Metal–organic framework (MOF) as a template for syntheses of nanoporous carbons as electrode materials for supercapacitor, Carbon 48 (2010) 456–463.
[32] Y. Liu, Z. Wang, Y. Zhong, M. Tade, W. Zhou, Z. Shao, Molecular design of mesoporous $NiCo_2O_4$ and $NiCo_2S_4$ with sub-micrometer-polyhedron architectures for efficient pseudocapacitive energy storage, Adv. Funct. Mater. 27 (2017) 1701229.
[33] H. Jia, J. Sun, X. Xie, K. Yin, L. Sun, Cicada slough-derived heteroatom incorporated porous carbon for supercapacitor: Ultra-high gravimetric capacitance, Carbon 143 (2019) 309–317.
[34] G. Murali, S. Harish, S. Ponnusamy, J. Ragupathi, H.A. Therese, M. Navaneethan, C. Muthamizhchelvan, Hierarchically porous structured carbon derived from peanut shell as an enhanced high rate anode for lithium ion batteries, Appl. Surf. Sci. 492 (2019) 464–472.
[35] M.A. Worsley, M.D. Merrill, S. Charnvanichborikarn, S.O. Kucheyev, J.H. Satcher, M. Stadermann, J. Biener, T.F. Baumann, Thick, binder-free carbon-nanotube-based electrodes for high power applications, ECS J. Solid State Sci. 2 (2013) M3140–M3144.
[36] Q. Wang, Q. Cao, X. Wang, B. Jing, H. Kuang, L. Zhou, A high-capacity carbon prepared from renewable chicken feather biopolymer for supercapacitors, J. Power Sources 225 (2013) 101–107.
[37] L. Wei, G. Yushin, Electrical double layer capacitors with activated sucrose-derived carbon electrodes, Carbon 49 (2011) 4830–4838.
[38] Y. Teng, K. Liu, R. Liu, Z. Yang, L. Wang, H. Jiang, R. Ding, E. Liu, A novel copper nanoparticles/bean dregs-based activated carbon composite as pseudocapacitors, Mater. Res. Bull. 89 (2017) 33–41.
[39] J.-W. Wang, Y. Chen, B.-Z. Chen, A synthesis method of MnO_2/activated carbon composite for electrochemical supercapacitors, J. Electrochem. Soc. 162 (2015) A1654–A1661.
[40] J. Yan, T. Wei, B. Shao, F. Ma, Z. Fan, M. Zhang, C. Zheng, Y. Shang, W.Z. Qian, F. Wei, Electrochemical properties of graphene nanosheet/carbon black composites as electrodes for supercapacitors, Carbon 48 (2010) 1731–1737.
[41] S. Maitra, N. Bandyopadhyay, S. Das, A.J. Pal, J. Pramanik, Non-isothermal decomposition kinetics of alkaline earth metal carbonates, J. Am. Ceram. Soc. 90 (2007) 1299–1303.
[42] T.A. Utigard, M. Wu, G. Plascencia, T. Marin, Reduction kinetics of Goro nickel oxide using hydrogen, Chem. Eng. Sci. 60 (2005) 2061–2068.
[43] K.S. Abdel-Halim, M.H. Khedr, M.I. Nasr, M.S. Abdel-wahab, Carbothermic reduction kinetics of nanocrystallite Fe_2O_3/NiO composites for the production of Fe/Ni alloy, J. Alloys Compd. 463 (2008) 585–590.
[44] S. Yao, Y. Zhu, S. He, L. Nie, Handbook of Chemical Reactions of Elements, Hunan Education Publishing House, Changsha, 1998, p. 1311.
[45] T. Otowa, R. Tanibata, M. Itoh, Production and adsorption characteristics of MAXSORB: High-surface-area active carbon, Gas Sep. Purif. 7 (1993) 241–245.
[46] J. Romanos, M. Beckner, T. Rash, L. Firlej, B. Kuchta, P. Yu, G. Suppes, C. Wexler, P. Pfeifer, Nanospace engineering of KOH activated carbon, Nanotechnology 23 (2011) 015401.
[47] N. Raghavan, S. Thangavel, G. Venugopal, A short review on preparation of graphene from waste and bioprecursors, Appl. Mater. Today 7 (2017) 246–254.
[48] K. Mukhopadhyay, M. Sharon, Glassy carbon from camphor - a natural source, Mater. Chem. Phys. 49 (1997) 105–109.
[49] B. Qi, X. He, G. Zeng, Y. Pan, G. Li, G. Liu, Y. Zhang, W. Chen, Y. Sun, Strict molecular sieving over electrodeposited 2D-interspacing-narrowed graphene oxide membranes, Nat. Commun. 8 (2017) 825.
[50] S. Vilvanathan, S. Shanthakumar, Ni^{2+} and Co^{2+} adsorption using Tectona grandis biochar: kinetics, equilibrium and desorption studies, Environ. Technol. 39 (2017) 464–478.
[51] M. Zhong, Y. Zhao, J.-R. Zhai, L.-J. Jin, H.-Q. Hu, Z.-Q. Bai, W. Li, Effects of nickel additives with different anions on the structure and pyrolysis behavior of Hefeng coal, Fuel Process. Technol. 193 (2019) 273–281.
[52] D. Lozano-Castelló, J.M. Calo, D. Cazorla-Amorós, A. Linares-Solano, Carbon activation with KOH as explored by temperature programmed techniques, and the effects of hydrogen, Carbon 45 (2007) 2529–2536.
[53] Y. Li, Q. Fu, M. Flytzani-Stephanopoulos, Low-temperature water-gas shift reaction over Cu- and Ni-loaded cerium oxide catalysts, Appl. Catal. B 27 (2000) 179–191.
[54] H. Liu, T. Chen, D. Chang, D. Chen, H. He, R.L. Frost, Catalytic cracking of tar derived from rice hull gasification over palygorskite-supported Fe and Ni, J. Mol. Catal. A Chem. 363–364 (2012) 304–310.